

# Real-time simulation of flux qubits used for quantum annealing

Madita Willsch,<sup>1,2</sup> Dennis Willsch,<sup>1,2</sup> Fengping Jin,<sup>1</sup> Hans De Raedt,<sup>3</sup> and Kristel Michielsen<sup>1,2</sup>

<sup>1</sup>*Institute for Advanced Simulation, Jülich Supercomputing Centre,  
Forschungszentrum Jülich, D-52425 Jülich, Germany*

<sup>2</sup>*RWTH Aachen University, D-52056 Aachen, Germany*

<sup>3</sup>*Zernike Institute for Advanced Materials,  
University of Groningen, Nijenborgh 4, NL-9747 AG Groningen, The Netherlands*

(Dated: September 3, 2022)

The real-time dynamics of systems with up to three SQUIDs is studied by numerically solving the time-dependent Schrödinger equation. The numerical results are used to scrutinize the mapping of the flux degrees of freedom onto two-level systems (the qubits) as well as the performance of the intermediate SQUID as a tunable coupling element. It is shown that the two-level representation yields a good description of the flux dynamics during quantum annealing, and the presence of the tunable coupling element does not have negative effects on the overall performance. Additionally, data obtained from a two-level spin dynamics simulation of quantum annealing is compared to experimental data produced by the D-Wave 2000Q quantum annealer. The effects of finite temperature are incorporated in the simulation by coupling the qubit-system to a bath of spin-1/2 particles. It is shown that including an environment modeled as non-interacting two-level systems that couple only to the qubits can produce data which matches the experimental data much better than the simulation data of the isolated qubits, and better than data obtained from a simulation including an environment modeled as interacting two-level systems coupling to the qubits.

Keywords: quantum computation; superconducting qubits; quantum annealing; SQUID; product-formula algorithm; optimization problems

## I. INTRODUCTION

The theoretical description of quantum information processors is usually limited to ideal two-level systems (qubits)[1]. However, almost all currently popular technologies such as superconducting circuits, ion traps, quantum dots, etc. employ physical devices which are only approximately described by two-level systems.

For the gate-based model of quantum computing, there is a very large body of theoretical work which focuses on detecting and correcting errors in quantum information processors that are built from ideal two-level systems. In contrast, there are only a few quantitative studies of the impact of the levels which have been omitted in the two-level description on the performance of the quantum information processor.

Recently, we published the results of such a study for superconducting transmons [2] that are used in the IBM Q processors [3]. Simulations of the transmon model revealed the presence of significant errors, not present in the approximate two-level description.

In this paper, we present a study, similar in spirit to Ref. [2], of the superconducting quantum interference devices (SQUIDs) that are used as qubits in the D-Wave quantum annealer. Specifically, by solving the time-dependent Schrödinger equation (TDSE) of up to three coupled SQUIDs using the flux degrees of freedom and the associated momenta, we study the effect of mapping the model in terms of flux degrees of freedom onto a spin-1/2 model. Our simulation model includes the SQUID that couples the two other SQUIDs which serve as the two qubits and, disregarding the fact that we simulate the model at zero temperature instead of finite temper-

ature, accounts for all effects such as cross-talk between the SQUIDs or population of higher levels not included in the two-level approximation and effects due to the presence of the SQUID functioning as the tunable coupling element. Because the simulation model includes all these effects, we focus on a small system of three SQUIDs, whose simulation already requires very extensive computational work.

We find that the effects due to the presence of higher levels and the coupling SQUID, although present, do not have a strong influence on the final ground-state probability and the quantum annealing process compared to quantum annealing with ideal two-level systems.

We observed that the frequency of finding the ground state of the two-qubit system reported by the D-Wave machine can be significantly less than the one obtained by simulation performed at zero temperature. We remove the latter constraint by adding interactions between the ideal qubits and an environment of spin-1/2 particles, representing e.g. a heat bath or a collection of defects. We simulate the annealing process in the presence of such an environment by solving the TDSE of the whole system, i.e. without any further approximation. We demonstrate that accounting for the coupling to the environment in this manner can significantly reduce the differences between the experimental data and the simulation data for the frequency of finding the ground state of the two-qubit systems.

The structure of the paper is as follows. In Sec. II, we give a short introduction to quantum annealing and its relation to optimization problems. Section III contains a description of the SQUID-based model which we simulate. The mapping of the model onto the two-level

system is given in Sec. IV. The dynamics of the SQUID-based model are simulated by solving the TDSE. The simulation method is described in Sec. V, and the results of the simulation are presented in Sec. VI. Subsequently, in Sec. VII, we describe the two different models for the baths of spin-1/2 particles coupled to the qubit system and discuss the simulation and its results in comparison to data obtained from the D-Wave 2000Q. Finally, we conclude with a summary in Sec. VIII.

## II. THEORETICAL BACKGROUND

In general, the Hamiltonian describing a quantum annealing process can be written as

$$H(s) = A(s)H_{\text{init}} + B(s)H_{\text{final}}, \quad (1)$$

where  $H_{\text{init}}$  is the initial Hamiltonian whose ground state defines the state in which the system is prepared initially,  $H_{\text{final}}$  denotes the Hamiltonian at the end of the annealing process and whose ground state is the one to be determined,  $s = t/t_a \in [0, 1]$ , is the rescaled (dimensionless) time, and  $t_a$  is the total annealing time. The functions  $A(s)$  and  $B(s)$  determine the annealing scheme and satisfy  $|A(0)| \gtrsim 1$ ,  $B(0) \approx 0$  and  $A(1) \approx 0$ ,  $|B(1)| \gtrsim 1$  (in appropriate units). The adiabatic theorem [4] states that the system stays in the ground state of the current Hamiltonian  $H(s)$  during the process if  $t_a \rightarrow \infty$  such that for  $s = 1$  the system is in the ground state of  $H_{\text{final}}$ .

Let  $\Delta E(s)$  denote the difference between the energy of the ground state and the first excited state, and let  $\Delta E = \min_s \Delta E(s)$  denote the minimal energy gap during the annealing process. If the energy gap  $\Delta E(s)$  does not become too small during the evolution, a finite  $t_a$  can be sufficient for the system to stay in the ground state with high probability.

Quantum annealing can be used to solve optimization problems that can be mapped onto a Hamiltonian  $H_{\text{final}}$ . The class of so-called quadratic unconstrained binary optimization problems (QUBOs) can be mapped onto Ising-spin Hamiltonians of the form

$$H_{\text{QUBO}} = -\sum_{k=1}^N h_k S_k - \sum_{1 \leq j < k} J_{jk} S_j S_k, \quad (2)$$

where  $N$  is the number of spins,  $h_k, J_{jk} \in \mathbb{R}$  define the particular QUBO, and  $S_k \in \{-1, 1\}$  are the spin variables. The set  $\{S_k\}$  of variables that minimize Eq. (2) give the solution of the QUBO.

Quantum annealing can, at least in principle, find (one of) the ground state(s) of the Ising-spin Hamiltonian Eq. (2) [5], or, equivalently, solve the corresponding QUBO. For this purpose, the two-valued variables  $S_k$  are replaced by the Pauli-Z matrices  $\sigma_k^z$  with eigenvalues  $\pm 1$  and eigenstates  $|\uparrow\rangle$  and  $|\downarrow\rangle$  such that the Hamiltonian in

Eq. (2) transforms to

$$H_{\text{Ising}} = -\sum_{k=1}^N h_k \sigma_k^z - \sum_{1 \leq j < k} J_{jk} \sigma_j^z \sigma_k^z. \quad (3)$$

The eigenstates of Eq. (3), which are product states of the  $\sigma^z$ -eigenstates, define the so-called computational basis. The ground state of Hamiltonian Eq. (3) can then be found by using quantum annealing with  $H_{\text{Ising}}$  as  $H_{\text{final}}$  in Eq. (1). A convenient choice for the initial Hamiltonian is the Hamiltonian for spins in transverse fields

$$H_{\text{trans}} = -\sum_{k=1}^N \sigma_k^x, \quad (4)$$

where  $\sigma^x$  is the Pauli-X matrix. The ground state of this Hamiltonian is given by the product state  $|+\cdots+\rangle$ , with  $|+\rangle = (|\uparrow\rangle + |\downarrow\rangle)/\sqrt{2}$ .

It is instructive to consider the simplest case  $N = 1$ , i.e., one spin, in which case the Landau-Zener theory applies [6, 7]. This theory describes a spin-1/2 system subject to a linearly increasing magnetic field  $h = vt$  where  $t$  varies from  $-\infty$  to  $\infty$  and  $v$  denotes the sweep velocity (all in appropriate units). The Hamiltonian is given by

$$H_{\text{LZ}}(t) = -h'_x \sigma^x - vt \sigma^z. \quad (5)$$

The probability for the system to end up in its ground state for  $t \rightarrow \infty$  is given by [6, 7]

$$P = 1 - e^{-a(\Delta E)^2/v}, \quad (6)$$

where  $a$  is a constant. From Eq. (6), it follows that  $P \rightarrow 1$  if  $\Delta E/\sqrt{v} \gg 1$ . Therefore, if the field is swept adiabatically, after the annealing process has completed, the system is in its ground state. If we use  $s = (1 + t/t_a)/2$  for  $t \in [-t_a, t_a]$  and  $h = vt_a$ , the Landau-Zener Hamiltonian can be written as

$$H_{\text{LZ}}(s) = -h'_x \sigma^x - h(2s - 1) \sigma^z. \quad (7)$$

Using Eqs. (3) and (4), the Hamiltonian for linear annealing ( $A(s) = h_x(1 - s)$ ,  $B(s) = s$ ) for a single spin is given by

$$H_{\text{AN}}(s) = -(1 - s)h_x \sigma^x - sh_z \sigma^z, \quad (8)$$

which can be mapped onto the Landau-Zener Hamiltonian  $H_{\text{LZ}}(s)$  if and only if  $|h_x| = |h_z|$  with  $h = -|h_z|/\sqrt{2}$  and  $h'_x = -h_z/\sqrt{2}$ . Although the mapping holds in a very restricted region only and the Landau-Zener theory applies for  $\Delta E(t \rightarrow \infty) \gg \Delta E$  (which is not guaranteed in general and not necessarily true in the cases that we investigate in this paper), it illustrates the basic features of quantum annealing.

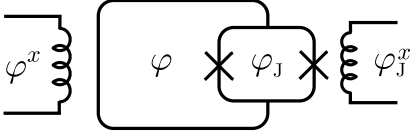


FIG. 1. Sketch of a SQUID with CJJ-loop. The magnetic fluxes  $\varphi$  and  $\varphi_J$  are the dynamical variables of the system. The external fluxes  $\varphi^x$  and  $\varphi_J^x$  are used to control the operation of the device.

### III. SQUID MODEL

Equations (3) and (4) are the Hamiltonians also used to formulate optimization problems for the quantum annealer manufactured by D-Wave Systems Inc. [8]. By design, the parameters of the final Hamiltonian are restricted to  $h_k \in [-2, 2]$  and  $J_{jk} \in [-1, 1]$ , and the connectivity is given by the Chimera graph such that, in the notation of Eq. (2), some  $J_{jk}$  cannot be specified and are fixed to zero [9]. D-Wave's quantum annealer consists of SQUIDs which are approximately described by two-level systems which can be mapped onto the sum of the Ising-spin Hamiltonian Eq. (3) and the spin Hamiltonian with transverse fields Eq. (4) [10].

In this paper, we consider a more general model for a system of three SQUIDs, two of which correspond to the two qubits and the third corresponds to the tunable coupler element. The qubits are defined by the subspace of the two lowest-energy states of a SQUID with a compound Josephson junction (CJJ) loop. Including the CJJ-loop leads effectively to a tunable Josephson junction.

Figure 1 shows the circuit of a SQUID with CJJ-loop which is used as a building block for the qubits and the effective coupling between the qubits in the D-Wave machine. The two qubit states correspond to the left-circulating and right-circulating persistent current in the superconducting (main) loop, and the tunable Josephson junction is used to control the annealing process. For the coupler element, the tunable Josephson junction results in the tunable coupling strength [11].

The Hamiltonian of a SQUID with CJJ-loop is given by [10, 12, 13]

$$H_{\text{SQUID}} = -E_C \partial_\varphi^2 + E_L \frac{(\varphi - \varphi^x)^2}{2} - E_{C_J} \partial_{\varphi_J}^2 + E_{L_J} \frac{(\varphi_J - \varphi_J^x)^2}{2} - E_J \cos(\varphi) \cos\left(\frac{\varphi_J}{2}\right), \quad (9)$$

where  $\varphi = 2\pi\Phi/\Phi_0 = 2e\Phi$  (we use  $\hbar = 1$ ) is the dimensionless magnetic flux in the main loop and  $\varphi_J$  the dimensionless magnetic flux in the CJJ-loop.  $\Phi_0$  denotes the magnetic flux quantum and  $e$  is the electron charge. After mapping onto a spin-1/2 model (see Sec. IV), the external fluxes  $\varphi^x$  and  $\varphi_J^x$  control the parameters of the final Hamiltonian given in Eq. (3) and determine the an-

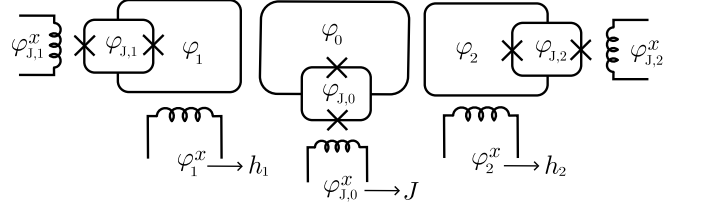


FIG. 2. Sketch of three SQUIDs to realize a tunable coupling. The magnetic fluxes  $\varphi_i$  and  $\varphi_{J,i}$  are the dynamical variables of the system. The external fluxes  $\varphi_i^x$  and  $\varphi_{J,i}^x$  are used to control the operation of the device. The parameters  $\varphi_1^x$ ,  $\varphi_2^x$  and  $\varphi_{J,0}^x$  determine the values of the parameters  $h_1$ ,  $h_2$  and  $J$  of the spin-1/2 model Eq. (3), respectively.

nealing process [9, 14].  $E_C$  and  $E_{C_J}$  are capacitive energies,  $E_L$  and  $E_{L_J}$  are inductive energies, and  $E_J$  is the Josephson energy. For an uncoupled SQUID, the inductive energy  $E_L$  is given by  $E_L = 1/(4e^2 L)$ , where  $L = L_{\text{main}} + L_J/4$  [10] is the qubit/coupler inductance.

#### A. Total Hamiltonian

A tunable coupling constant  $J_{jk}$  is realized by inserting a SQUID as a coupler element between the other two SQUIDs [11, 15]. For the SQUID that functions as the coupler element, we denote the flux in the CJJ-loop by  $\varphi_{J,0}$  and the one in the main loop by  $\varphi_0$ . Accordingly, energies that correspond to the coupler main loop are labeled by an index “0”, and those that correspond to the coupler CJJ-loop by an index “J,0”. The external control flux  $\varphi_{J,0}^x$  can be used to tune the coupling strength between the SQUIDs. We label the fluxes of the SQUIDs corresponding to the qubits with indices “1” and “2”, respectively. Since their energies and their external fluxes  $\varphi_J^x$  are assumed to be equal, we drop the indices “1” and “2” in these cases. Although the external fluxes  $\varphi_1^x$ ,  $\varphi_2^x$  and  $\varphi_J^x$  depend on time, we do not write this explicitly for reasons of readability. A sketch of the complete system is shown in Fig. 2.

By coupling SQUIDs, the inductive energies change such that they are given by  $E_L(1 + M^2/(LL_{\text{eff}}))$  for the SQUIDs representing the qubits, and  $E_{L_{\text{eff}}} = E_{L_0}L_0/L_{\text{eff}}$  for the coupler where  $L_{\text{eff}} = L_0 - 2M^2/L$  is the effective inductance of the coupler element, and  $M$  is the mutual inductance between the coupler and the other SQUIDs' main loops. In addition to the modified Hamiltonians of the three SQUIDs, the interaction terms

$$H_{\text{int}} = \frac{M}{L_{\text{eff}}} E_L (\varphi_1 - \varphi_1^x) (\varphi_0 - \varphi_0^x) + \frac{M}{L_{\text{eff}}} E_L (\varphi_2 - \varphi_2^x) (\varphi_0 - \varphi_0^x) + \frac{M^2}{LL_{\text{eff}}} E_L (\varphi_1 - \varphi_1^x) (\varphi_2 - \varphi_2^x), \quad (10)$$

have to be included [16]. The tunable coupler can be operated without an external flux in the coupler main

loop [11]. Therefore, we set  $\varphi_0^x = 0$ . Collecting all terms, the total Hamiltonian is given by

$$\begin{aligned}
H_{\text{total}} = \sum_{i=1}^2 \left[ -E_J \cos(\varphi_i) \cos\left(\frac{\varphi_{J,i}}{2}\right) + E_{LJ} \frac{(\varphi_{J,i} - \varphi_J^x)^2}{2} \right. \\
\left. - E_{CJ} \partial_{\varphi_{J,i}}^2 + E_L \left(1 + \frac{M^2}{LL_{\text{eff}}}\right) \frac{(\varphi_i - \varphi_i^x)^2}{2} - E_C \partial_{\varphi_i}^2 \right] \\
+ E_{L_{\text{eff}}} \frac{\varphi_0^2}{2} - E_{C_0} \partial_{\varphi_0}^2 + E_{L_{J,0}} \frac{(\varphi_{J,0} - \varphi_J^x)^2}{2} \\
- E_{C_{J,0}} \partial_{\varphi_{J,0}}^2 - E_{J_0} \cos(\varphi_0) \cos\left(\frac{\varphi_{J,0}}{2}\right) \\
+ \frac{M}{L_{\text{eff}}} E_L (\varphi_1 - \varphi_1^x) \varphi_0 + \frac{M}{L_{\text{eff}}} E_L (\varphi_2 - \varphi_2^x) \varphi_0 \\
+ \frac{M^2}{LL_{\text{eff}}} E_L (\varphi_1 - \varphi_1^x) (\varphi_2 - \varphi_2^x). \quad (11)
\end{aligned}$$

This is the final Hamiltonian for which we solve the TDSE without further simplification.

### B. Effective coupling

The idea of inserting the coupler element is that it leads to a tunable effective coupling between the other two SQUIDS [11, 15, 16] such that the interaction Hamiltonian takes the form

$$H_{\text{int}}^{\text{eff}} = C(\varphi_{J,0}^x) \varphi_1 \varphi_2, \quad (12)$$

where  $C(\varphi_{J,0}^x)$  is the effective coupling strength tunable by the external flux  $\varphi_{J,0}^x$  of the coupler CJJ-loop.

To derive an approximate effective Hamiltonian that exhibits such a coupling term, we first replace the flux of the coupler CJJ-loop  $\varphi_{J,0}$  by its approximate expectation value. To obtain this expectation value, we expand the Hamiltonian of the SQUID given in Eq. (9) to second order in  $\varphi_{J,0} - \varphi_{J,0}^x$  and set  $\varphi_0 = 0$ . The resulting Hamiltonian describes a shifted harmonic oscillator:

$$\begin{aligned}
H_{\text{co}} = \frac{E'_{L_{J,0}}}{2} \left( \varphi_{J,0} - \left( \varphi_{J,0}^x - \frac{2E_{J_0} \sin(\varphi_{J,0}^x/2)}{4E'_{L_{J,0}}} \right) \right)^2 \\
- E_{C_{J,0}} \partial_{\varphi_{J,0}}^2, \quad (13)
\end{aligned}$$

where  $E'_{L_{J,0}} = E_{L_{J,0}} + E_{J_0} \cos(\varphi_{J,0}^x/2)/4$ . The expectation value of  $\varphi_{J,0}$  in its ground state can thus be identified as

$$\langle \varphi_{J,0} \rangle = \varphi_{J,0}^x - \frac{2E_{J_0} \sin(\varphi_{J,0}^x/2)}{4E_{L_{J,0}} + E_{J_0} \cos(\varphi_{J,0}^x/2)}. \quad (14)$$

With  $\varphi_{J,0}$  replaced by  $\langle \varphi_{J,0} \rangle$ , we can find a matrix  $T$  such that the transformation

$$H^{\text{eff}} = e^{iT(t)} H_{\text{total}} e^{-iT(t)} + i \left( \frac{d}{dt} e^{iT(t)} \right) e^{-iT(t)}, \quad (15)$$

of the total Hamiltonian, with  $\varphi_{J,0}$  replaced by its expectation value, yields an effective Hamiltonian which contains an interaction term of the form Eq. (12). Choosing

$$T = T(t) = i \frac{M}{L(1 + \beta_{\text{eff}})} (\varphi_1 - \varphi_1^x + \varphi_2 - \varphi_2^x) \partial_{\varphi_0}, \quad (16)$$

where the external fluxes  $\varphi_1^x$  and  $\varphi_2^x$  depend on time,

$$\beta_{\text{eff}} = \frac{E_{J_0}}{E_{L_{\text{eff}}}} \cos\left(\frac{\langle \varphi_{J,0} \rangle}{2}\right), \quad (17)$$

and expanding

$$\cos\left(\varphi_0 - \frac{M}{L(1 + \beta_{\text{eff}})} (\varphi_1 - \varphi_1^x + \varphi_2 - \varphi_2^x)\right), \quad (18)$$

to second order in (the products of)  $\varphi_0$ ,  $\varphi_1 - \varphi_1^x$ , and  $\varphi_2 - \varphi_2^x$ , we obtain the effective Hamiltonian

$$\begin{aligned}
H^{\text{eff}} = \sum_{i=1}^2 \left[ E_L \left( 1 + \frac{M^2}{LL_{\text{eff}}} \frac{\beta_{\text{eff}}}{1 + \beta_{\text{eff}}} \right) \frac{\varphi_i^2}{2} \right. \\
\left. - E_C \partial_{\varphi_i}^2 - E_J \cos(\varphi_i) \cos\left(\frac{\varphi_{J,i}}{2}\right) \right. \\
\left. - E_{CJ} \partial_{\varphi_{J,i}}^2 + E_{LJ} \frac{(\varphi_{J,i} - \varphi_J^x)^2}{2} \right] \\
+ \sum_{i=1}^2 \left[ -E_L \left( 1 + \frac{M^2}{LL_{\text{eff}}} \frac{\beta_{\text{eff}}}{1 + \beta_{\text{eff}}} \right) \varphi_i^x \varphi_i \right] \\
+ \sum_{i=1}^2 \left[ -E_L \frac{M^2}{LL_{\text{eff}}} \frac{\beta_{\text{eff}}}{1 + \beta_{\text{eff}}} \varphi_{j \neq i}^x \varphi_i \right] \\
+ E_L \frac{M^2}{LL_{\text{eff}}} \frac{\beta_{\text{eff}}}{1 + \beta_{\text{eff}}} \varphi_1 \varphi_2 \\
- \left( E_{C_0} + \frac{2E_C M^2}{L^2(1 + \beta_{\text{eff}})^2} \right) \partial_{\varphi_0}^2 \\
+ \frac{M}{L(1 + \beta_{\text{eff}})} \left( i \frac{d}{dt} (\varphi_1^x + \varphi_2^x) - 2E_C (\partial_{\varphi_1} + \partial_{\varphi_2}) \right) \partial_{\varphi_0} \\
+ E_{L_{\text{eff}}} (1 + \beta_{\text{eff}}) \frac{\varphi_0^2}{2}. \quad (19)
\end{aligned}$$

In the basis defined by the transformation Eq. (15), we obtain the term  $C(\varphi_{J,0}^x) \varphi_1 \varphi_2$  where the dependence on  $\varphi_{J,0}^x$  is given via  $\langle \varphi_{J,0} \rangle$  in  $\beta_{\text{eff}}$  (see Eqs. (14) and (17)). The only coupling term between the coupler element and the other two SQUIDS that remains is the second last term in Eq. (19) which is expected to be much smaller than the previous coupling terms since  $E_C \ll E_L$ . We also find terms proportional to  $\varphi_{j \neq i}^x \varphi_i$ , meaning that the external fluxes  $\varphi_1^x$  and  $\varphi_2^x$  influence SQUID 2 and SQUID 1, respectively (which is also referred to as cross-talk [17, 18]).

During the annealing process, the external fluxes  $\varphi_J^x$  change in time such that the potentials for the fluxes in the main loops  $\varphi_i$ ,  $i = 1, 2$ , change from harmonic potentials with anharmonicity to double-well potentials.

The external fluxes  $\varphi_i^x$  can be used to bias one of the two wells, respectively, according to the chosen parameters  $h_i$ .

Note that none of the approximations made to derive Eq. (19) affect the simulation results, as these are obtained by solving the TDSE for Hamiltonian Eq. (11). Note that neither of the approximations made so far nor the mapping to the 2-level system are necessary for the simulation itself which is based on Eq. (11) only. However, these approximations are necessary for the mapping of  $J$  to  $\varphi_{J,0}^x$  and the comparison between the simulations of the SQUID-based model and the model of 2-level systems.

#### IV. MAPPING TO THE 2-LEVEL SYSTEM

For further analytical investigation, to find a relation between  $\varphi_{J,0}^x$  and  $J_{12}$  ( $= J$  for two qubits) and a condition for  $\varphi_i^x$ , we perform the mapping to a model of 2-level systems.

Since the mapping to a 2-level system is identical for the two SQUIDs, for simplicity, we do not write the SQUID indices here. The two lowest-energy states  $|g\rangle$  and  $|e\rangle$  of each SQUID for  $\varphi^x = 0$  define the computational subspace [10]. We obtain them by diagonalizing the first part in square brackets of Eq. (19) in  $\varphi$ - and  $\varphi_J$ -space (see Sec. V for the definition of the discretized basis).

Note that, the first summand given in Eq. (19) contains an effective change of the inductive energy depending on the value chosen for  $\varphi_{J,0}^x$  (because  $\beta_{\text{eff}}$  depends on it). Therefore, the definition of the computational subspace changes with the coupling strength. This leads to slightly different annealing schemes, i.e., a dependence of  $A(s)$  on  $\varphi_{J,0}^x$ , as observed experimentally [10, 11].

The computational basis states  $|\uparrow\rangle$  and  $|\downarrow\rangle$  are defined as the eigenstates of the operator  $\varphi$  (and thus of the second part in square brackets in Eq. (19) inside the computational subspace  $\text{span}\{|g\rangle, |e\rangle\}$ ). We obtain

$$|\uparrow\rangle = a|g\rangle + b|e\rangle = \int_{-\infty}^{\infty} \int_{-\infty}^{\infty} d\varphi d\varphi_J u(\varphi, \varphi_J) |\varphi \varphi_J\rangle, \quad (20)$$

$$|\downarrow\rangle = a|g\rangle - b|e\rangle = \int_{-\infty}^{\infty} \int_{-\infty}^{\infty} d\varphi d\varphi_J d(\varphi, \varphi_J) |\varphi \varphi_J\rangle, \quad (21)$$

where  $|a| = |b| = 1/\sqrt{2}$  [10] and  $u(\varphi, \varphi_J)$  and  $d(\varphi, \varphi_J)$  are the resulting amplitudes of the states  $|\uparrow\rangle$  and  $|\downarrow\rangle$  in  $\varphi$ - and  $\varphi_J$ -space. The eigenvalues  $\pm I_p(s)$  of  $|\uparrow\rangle$  and  $|\downarrow\rangle$  correspond to the left- and right-circulating persistent current, respectively. Thus, in this subspace  $\tilde{E}_L \varphi = I_p(s) \sigma^z / 2e$  with  $\tilde{E}_L = E_L(1 + M^2/LL_{\text{eff}} \times \beta_{\text{eff}}/(1 + \beta_{\text{eff}}))$ , and the first contributions in square brackets in Eq. (19) are mapped to  $-\Delta(s)\sigma^x/2$  where  $\Delta(s) = E_1(s) - E_0(s)$  is the energy gap between the ground state  $|g\rangle$  and the first excited state  $|e\rangle$ .

To derive the coupling terms, we write the SQUID indices  $i$  again. For the terms in  $\sigma_i^z$  and  $\sigma_1^z \sigma_2^z$  to scale with the same annealing function  $B(s)$  [9],  $\varphi_i^x$  has to be set to

$$\varphi_i^x = h_i \gamma \frac{2e I_p(s) M^2}{L_{\text{eff}}}, \quad (22)$$

where  $\gamma = \max_{\varphi_{J,0}^x} \beta_{\text{eff}} E_L^2 / (1 + \beta_{\text{eff}}) \tilde{E}_L^2$ . Disregarding the contribution of the second last term in Eq. (19), we find that the Hamiltonian for  $\varphi_0$  effectively decouples from the qubit Hamiltonian, and thus, the effective qubit Hamiltonian can be written as

$$\begin{aligned} H^{\text{eff},q} \approx & - \sum_{i=1}^2 \left( \frac{\Delta(s)}{2} \sigma_i^x + h_i \gamma \frac{I_p^2(s) M^2}{L_{\text{eff}}} \sigma_i^z \right) \\ & - \frac{E_L}{\tilde{E}_L} \frac{I_p^2(s) M^4}{LL_{\text{eff}}} \frac{\beta_{\text{eff}}}{1 + \beta_{\text{eff}}} \gamma (h_1 \sigma_2^z + h_2 \sigma_1^z) \\ & + \frac{E_L^2}{\tilde{E}_L^2} \frac{I_p^2(s) M^2}{L_{\text{eff}}} \frac{\beta_{\text{eff}}}{1 + \beta_{\text{eff}}} \sigma_1^z \sigma_2^z. \end{aligned} \quad (23)$$

For all  $J \in [-1, 1]$ , we have

$$-\gamma = -\max_{\varphi_{J,0}^x} \frac{\beta_{\text{eff}}}{1 + \beta_{\text{eff}}} \frac{E_L^2}{\tilde{E}_L^2} \leq -J\gamma \leq \max_{\varphi_{J,0}^x} \frac{\beta_{\text{eff}}}{1 + \beta_{\text{eff}}} \frac{E_L^2}{\tilde{E}_L^2} = \gamma. \quad (24)$$

Thus, and because  $E_L^2 \beta_{\text{eff}}(\varphi_{J,0}^x) / \tilde{E}_L^2(\varphi_{J,0}^x) (1 + \beta_{\text{eff}}(\varphi_{J,0}^x))$  is monotonic, it is possible to find  $\varphi_{J,0}^x$  such that

$$\frac{\beta_{\text{eff}}(\varphi_{J,0}^x)}{1 + \beta_{\text{eff}}(\varphi_{J,0}^x)} \frac{E_L^2}{\tilde{E}_L^2(\varphi_{J,0}^x)} = -J\gamma, \quad (25)$$

for all  $J \in [-1, 1]$ , and Eq. (23) becomes

$$\begin{aligned} H^{\text{eff},q} \approx & - \sum_{i=1}^2 \frac{\Delta(s)}{2} \sigma_i^x - \gamma \frac{I_p^2(s) M^2}{L_{\text{eff}}} \left( \sum_{i=1}^2 h_i \sigma_i^z + J \sigma_1^z \sigma_2^z \right. \\ & \left. - \frac{\tilde{E}_L}{E_L} \frac{M^2}{LL_{\text{eff}}} J \gamma (h_1 \sigma_2^z + h_2 \sigma_1^z) \right), \end{aligned} \quad (26)$$

which has the structure of an Ising model in a transverse field. Comparing Eq. (26) to Eq. (3) and Eq. (4), we can identify  $A(s) = \Delta(s)/2$  and  $B(s) = \gamma I_p^2(s) M^2 / L_{\text{eff}}$ , and see that

$$\begin{aligned} H^{\text{eff},q} \approx & - A(s) (\sigma_1^x + \sigma_2^x) \\ & - B(s) \left( h_1 \sigma_1^z + h_2 \sigma_2^z + J \sigma_1^z \sigma_2^z \right. \\ & \left. - \frac{\tilde{E}_L}{E_L} \frac{M^2}{LL_{\text{eff}}} J \gamma (h_1 \sigma_2^z + h_2 \sigma_1^z) \right), \end{aligned} \quad (27)$$

where the last term only adds a small contribution since  $M^2 \ll LL_{\text{eff}}$ .

## V. SIMULATION

For the simulation of the time-evolution of the system defined by Eq. (11), we use the Suzuki-Trotter product-formula algorithm [19, 20] to numerically solve the TDSE

$$i\partial_t|\psi(t)\rangle = H(t)|\psi(t)\rangle. \quad (28)$$

The time-dependent Hamiltonian is discretized such that the state vector  $|\psi(t)\rangle$  can be updated by a time step  $\tau$  to  $|\psi(t+\tau)\rangle$  using the time-evolution operator  $U(t, t+\tau) = \exp(-i\tau H(t+\tau/2))$ . To implement the algorithm, we fix a basis for the description of  $|\psi(t)\rangle$  and a decomposition of the Hamiltonian  $H(t) = \sum_k A_k(t)$  such that

$$e^{-iH(t)\tau} \approx e^{-iA_1(t)\tau} e^{-iA_2(t)\tau} \dots e^{-iA_K(t)\tau} = U_{t,1}(\tau), \quad (29)$$

is a good approximation for sufficiently small  $\tau$ , and the update of the state vector can be performed with two-component updates only. For a detailed description of how to choose the  $A_k$ , see Ref. [20]. In our simulation, we use the second order approach given by

$$e^{-iH(t)\tau} \approx U_{t,1}(\tau/2) U_{t,1}^\dagger(-\tau/2). \quad (30)$$

Note that there is no need to diagonalize the Hamiltonian, or to store the full matrices representing the Hamiltonian or the time-evolution operator.

For the description of the state  $|\psi\rangle$ , the fluxes  $\varphi_i$  through the main loops are discretized, i.e., the wave function is defined at  $\lambda_i$  discrete points  $\varphi_{i\min} + l_i\Delta\varphi_i$ ,  $l_i = 0, \dots, \lambda_i - 1$ . By studying the convergence of the numerical results as a function of  $\lambda_i$  and  $\Delta\varphi_i$ , we find that  $\lambda_1 = \lambda_2 = 47$ ,  $-2.0 \leq \varphi_1, \varphi_2 \leq 2.0$ , and  $\lambda_0 = 31$ ,  $-1.0 \leq \varphi_0 \leq 1.0$  provide a good compromise between accuracy and computational work to solve the TDSE. Since  $E_{L_J} \gg E_J$  and  $E_{L_{J,0}} \gg E_{J_0}$ , the Hamiltonian for  $\varphi_{J,i}$  resembles an oscillator with small anharmonicity. In the harmonic oscillator basis, the evolution of  $\varphi_{J,i}$  can be well described with the 3 lowest states, and thus the fluxes  $\varphi_{J,i}$  through the CJJ-loops can be discretized in the harmonic oscillator basis and labeled by  $|m_i\rangle$ ,  $m_i = 0, 1, 2$ . In summary, the state  $|\psi\rangle$  is represented by

$$|\psi\rangle = \sum_{\substack{l_0, l_1, l_2, \\ m_0, m_1, m_2}} \phi_{l_0, m_0, l_1, m_1, l_2, m_2} |l_0 m_0 l_1 m_1 l_2 m_2\rangle, \quad (31)$$

where the amplitudes  $\phi_{l_0, m_0, l_1, m_1, l_2, m_2}$  are stored as an array of  $\lambda_1 \cdot \lambda_2 \cdot \lambda_0 \cdot 3^3 \approx 1.85 \times 10^6$  complex double precision numbers. To store this array, approximately 30 MB of memory is needed. Parallelization of the state updates is implemented using OpenMP. Testing with decreasing time steps  $\tau$  and studying the convergence, we find that for  $\tau = 1.5 \times 10^{-5}$  ns the results are sufficiently accurate. Due to this small time step, one quantum annealing run of 5 ns takes about 16 hours on a 24-core node of the supercomputer JURECA [21].

TABLE I. Device parameters of the Hamiltonian given in Eq. (11).

Parameter	Value	Parameter	Value
$E_C$	4.68 GHz	$E_{C_0}$	9.02 GHz
$E_L$	3.48 THz	$E_{L_0}$	15.67 THz
$E_{C_J}$	133.02 GHz	$E_{C_{J,0}}$	213.0 GHz
$E_{L_J}$	54.54 THz	$E_{L_{J,0}}$	354.18 THz
$E_J$	7.80 THz	$E_{J_0}$	18.72 THz
$M$	15.97 pH		

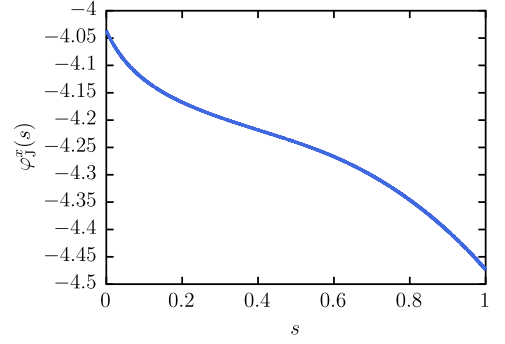


FIG. 3. (color online) The external flux  $\varphi_J^x$  as a function of the normalized annealing time  $s$ , as provided to us by D-Wave Systems Inc.

### A. Parameters

The parameters of the Hamiltonian Eq. (11) and the values of the time-dependent flux  $\varphi_J^x(s)$ , which determines the annealing scheme, were provided to us by D-Wave Systems Inc. [22]. The device parameters used in the simulation are slightly modified and listed in Table I and  $\varphi_J^x(s)$  is plotted in Fig. 3. The external fluxes  $\varphi_i^x$  and  $\varphi_{J,0}^x$  are computed from Eq. (22) and by solving Eq. (25) numerically for  $\varphi_{J,0}^x(J)$ .

Using the provided parameters, we compute the annealing scheme of a single SQUID by exact diagonalization. However, the resulting annealing scheme (data not shown) does not match the data of the annealing scheme provided to us by D-Wave Systems Inc. [22], see Fig. 4 (dashed lines). Better agreement between the two annealing schemes was found by using  $E_C = 4.68$  GHz (which was computed from the provided capacitance directly) instead of  $E_C = 5.85$  GHz (which includes an extra capacitance),  $E_{L_J} = 54538$  GHz instead of  $E_{L_J} = 73388$  GHz, and  $M = 15.97$  pH instead of  $M = 13.7$  pH, see Fig. 4 (solid lines). The disagreement in  $B(s)$  for small  $s$  could not be removed by slight variation of the model parameters. Changing  $\varphi_i^x$  would reduce the disagreement for the single-qubit terms, but at the same time Eq. (22) would be violated, effectively yielding different functions for the single-qubit and two-qubit  $\sigma^z$ -terms. Thus, we decided to keep  $\varphi_i^x$  as given by Eq. (22).

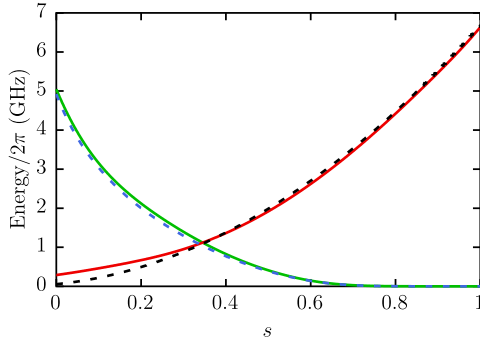


FIG. 4. (color online) The functions  $A(s)$  and  $B(s)$  of the annealing scheme as provided to us by D-Wave Systems Inc. (dashed lines) in comparison to the annealing scheme obtained from the full Hamiltonian for an uncoupled SQUID (solid lines).

### B. Estimation of the coupling strength and the annealing scheme

In order to map the full state Eq. (31) to the computational space, we have to trace out the degrees of freedom of the coupler element and project the resulting reduced density matrix onto the computational subspace. To do so, we discretize Eqs. (20) and (21) to obtain

$$|\uparrow\rangle = \sum_{l,m} u_{l,m} |lm\rangle, \quad (32)$$

$$|\downarrow\rangle = \sum_{l,m} d_{l,m} |lm\rangle, \quad (33)$$

for a single qubit, and accordingly the product states for the two-qubit states, and where  $u_{lm}$  and  $d_{lm}$  are the discretizations of  $u(\varphi, \varphi_J)$  and  $d(\varphi, \varphi_J)$ . Since this projection is not a unitary transformation, the trace of the projected density matrix  $\rho^{\text{comp}}$  will be less than one if there is leakage to higher levels, i.e., if there occur excitations to states outside the computational subspace. The deviation of the trace from one is a measure for the amount of leakage to higher levels.

To obtain the effective coupling strength we proceed as follows. We start with the ideal 2-level Hamiltonian (for simplicity with  $h_1 = h_2 = 0$ )

$$H_2(s) = -\frac{\Delta(s)}{2} (\sigma_1^x + \sigma_2^x) + C(s) \sigma_1^z \sigma_2^z, \quad (34)$$

where  $\Delta(s)$  and  $C(s)$  are to be determined by comparison with the data obtained by simulating the model Eq. (11). For fixed  $s \in [0, 1]$ , the evolution of the initial state  $|++\rangle = (|\uparrow\rangle + |\downarrow\rangle) \otimes (|\uparrow\rangle + |\downarrow\rangle) / 2$  and the expectation values  $\langle \sigma_1^\alpha \sigma_2^\beta \rangle$  for  $\sigma_i^\alpha, \sigma_i^\beta \in \{\mathbb{I}_i, \sigma_i^x, \sigma_i^y, \sigma_i^z\}$  can be calculated analytically. On the other hand, we can compute these expectation values directly from the simulation of the full Hamiltonian Eq. (11) based on the flux degrees of freedom with fixed  $s$ . We can then estimate  $\Delta(s)$  and  $C(s)$ , and thus the effective coupling strength and the

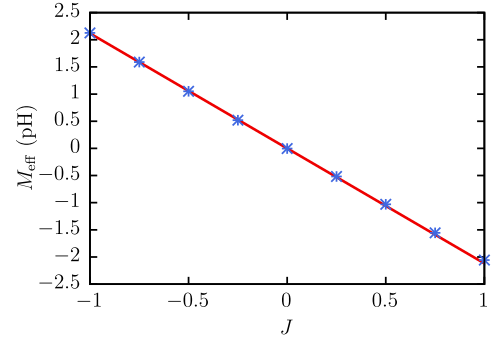


FIG. 5. (color online) Effective mutual inductance between the qubits as a function of the two-spin coupling  $J$ . Solid line: the expected behavior based on the analytical calculation presented in Sec. IV. Markers (asterisks): simulation data.

annealing scheme, by fitting the analytical expressions to the simulation data.

## VI. RESULTS

### A. Effective coupling

In order to assess the mapping between  $J$  and  $\varphi_{J,0}$  using Eq. (25), we first study the effective mutual inductance  $M_{\text{eff}}$  as a function of  $J$ . We utilize the method described in Sec. VB for various values of  $J$  and  $s = 1$  (such that  $\Delta(s) \approx 0$ ) to determine the coupling strength. In this case, the expectation value  $\langle \sigma_1^y \sigma_2^z \rangle = \sin(2C(1)t)$  can be used for fitting. The obtained value for  $C(1)$  for each  $J$  is then mapped onto the effective mutual inductance  $M_{\text{eff}}(J) = C(1)/I_p^2(1) = -J\gamma M^2/L_{\text{eff}}$  and plotted against  $J$ . The result for the effective inductance  $M_{\text{eff}}(J)$  between the qubits is presented in Fig. 5, and shows good agreement between the theoretical linear curve from the approximation and the simulation result. For  $J$  in the range  $[-1, 1]$ , we can reach all values for  $M_{\text{eff}}$  in  $[-M_{\text{eff,max}}, M_{\text{eff,max}}]$  to good precision and have thus obtained a transformation  $\varphi_{\text{co}}^x \leftrightarrow J$  such that the mapping  $J \leftrightarrow M_{\text{eff}}$  is linear. Therefore, we can expect that the mapping onto the 2-level system and the resultant mapping  $J \leftrightarrow \varphi_{\text{co}}^x$  work reasonably well.

### B. Comparison to the two-level system

The next step is to compare the overall performance and the success probabilities between the real-time simulation with the Hamiltonian given in Eq. (11) and the 2-level system. Figure 6 shows the effective annealing scheme (data points) obtained with the method described in Sec. VB, using the expectation value

$$\langle \sigma_1^z \sigma_2^z \rangle = \frac{2\Delta(s')C(s') \sin^2 \left( \sqrt{\Delta(s')^2 + C(s')^2} t \right)}{\Delta(s')^2 + C(s')^2}, \quad (35)$$



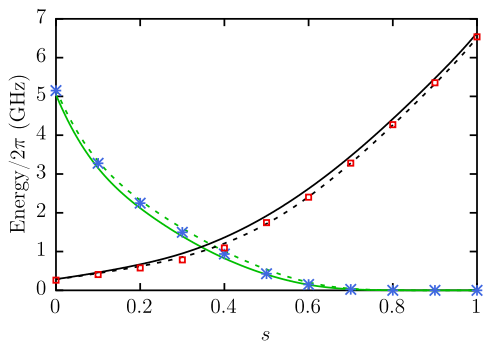


FIG. 6. (color online) Annealing scheme for an uncoupled single SQUID obtained using Eq. (9) (solid line), and including the effective shifts in the inductive energy encountered in Eq. (19) (dashed line) to show the effect of coupling on the annealing scheme. Asterisks (blue) and squares (red) are obtained from the simulation as described in Sec. IV with  $\Delta s = 0.1$ . Solid and dashed lines following the asterisks represent  $A(s)$ , and solid and dashed lines following the squares represent  $B(s)$ . The parameters are  $J = -1$ ,  $h_1 = h_2 = 0$ , where the choice of the latter is made to simplify the analytical calculation.

for the fitting of  $\Delta(s')$  and  $C(s')$ .

We find that the data points in Fig. 6 deviate from the annealing scheme for an uncoupled qubit (solid lines, obtained using Eq. (9)), but they are in better agreement with the annealing scheme obtained by using  $E_L(1 + M^2/(LL_{\text{eff}})\beta_{\text{eff}}/(1 + \beta_{\text{eff}}))$  instead of  $E_L$  (dashed lines). Note that for the computation of the annealing scheme, the single SQUID Hamiltonian Eq. (9) (and thus the term proportional to  $\sigma^z$ ) is used which gives the same function for  $B(s)$  as the term proportional to  $\sigma_1^z \sigma_2^z$  in the case of two coupled qubits because of the choice for  $\varphi^x$ . So we find, in agreement with our analytical calculation, that the effective coupling between the qubits induces a shift in the inductive energy, leading to shifts in the annealing scheme. The influence of the coupling on the inductive energy was also observed in experiments [11].

As mentioned in Sec. V, the amount of leakage to higher excited states can be computed by projecting the density matrix onto the computational subspace. The projected density matrix can also be used to obtain the probabilities of the computational basis states. As an illustration, in Fig. 7 we show the results for  $J = -1$ ,  $h_1 = 0.96$ ,  $h_2 = 0.94$ . The total annealing time was set to  $t_a = 5$  ns, which is much less than for the D-Wave processors (a few  $\mu s$ ), but for comparison with the 2-level description, this difference to the experiment has no significance.

As seen from Fig. 7, there are small deviations from the probabilities obtained from the 2-level representation. Some leakage which has its maximum at about  $s = 0.6$ , where the change in the probabilities of the computational states is strongest, can also be observed. In general, the evolutions of both the full model and its 2-level approximation show the same features, the final

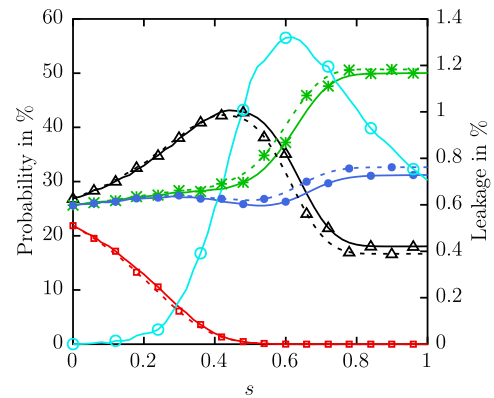


FIG. 7. (color online) Probabilities of the four computational states  $|\uparrow\uparrow\rangle$  (black triangles),  $|\uparrow\downarrow\rangle$  (green asterisks),  $|\downarrow\uparrow\rangle$  (blue bullets), and  $|\downarrow\downarrow\rangle$  (red squares) during the annealing process for the 2-level system (dashed lines) and the full system (solid lines). Markers are used to better distinguish the lines of the different states. For the data from the simulation of the 2-level model, every 120th data point is plotted with a marker and for the data from the simulation of the full system, every 6th point is plotted with a marker. For the full system, additionally the probability of leakage (cyan circles) is shown using the right  $y$ -axis. The annealing time was set to  $t_a = 5$  ns. The parameters are  $J = -1$ ,  $h_1 = 0.96$  and  $h_2 = 0.94$ .

probability differing only slightly. In the example shown here, the success probability is higher for the ideal 2-level system. However, Fig. 8 shows that there are also cases in which the success probability is lower for the 2-level system. Note that the annealing process does not start with equal probability for all states because we start the annealing in the ground state of the system instead of in the state  $|++\rangle = |+\rangle_1 \otimes |+\rangle_2$ , since for  $B(s=0) > 0$ , the ground state of the spin-1/2 model Eq. (3) is not exactly the state  $|++\rangle$  but a superposition of all basis states. A simulation of the 2-level model comparing the annealing processes with the two different initial states shows deviations during the annealing process, but there is no significant difference in the success probability (data not shown).

In summary, we observed effects of the coupling on the annealing scheme, and some amount of leakage to higher levels. The important question, however, is whether these effects have consequences on the final success probability. Figure 8 shows the success probability for many different problems (defined in Appendix A) as a function of the minimal energy gap between the ground state and the first excited state during the annealing process. As can be seen in Fig. 8, for most of the investigated cases, the effects on the success probability of using a subspace of a larger system as qubit instead of an ideal 2-level representation are rather small. The data points generated by the simulation based on Eq. (11) (black circles) show, apart from a few exceptions, only small deviations from the data points of the ideal 2-level system (red bullets). Note that the success probability can as well be enhanced as reduced compared to the ideal system.



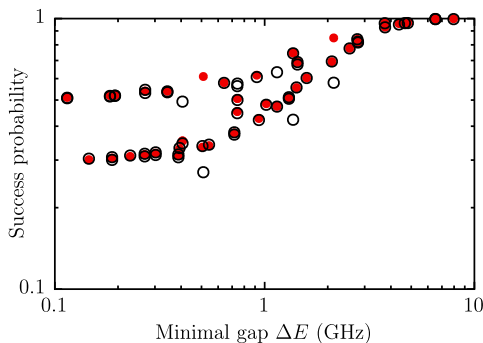


FIG. 8. (color online) Success probability of an annealing process as a function of the minimal energy gap  $\Delta E = E_1 - E_0$  (computed from the two-level system representation) during the annealing process. Each data point represents another problem, i.e., other values for the parameters  $h_1$ ,  $h_2$  and  $J$ . A list with all cases is given in Appendix A. Bullets (red) show the results for the 2-level system, and circles (black) originate from the simulation of the full system.

As noted in Ref. [17, 18] and confirmed by our analytical calculation in Sec. IV, there is some cross-talk between the qubits, leading to small offsets in the parameters  $h_i$ . Furthermore, a dependence of the annealing scheme on the parameter  $\varphi_{J,0}^x$  was found, also leading to small discrepancies between the ideal 2-level representation and the full system. Additionally, for the mapping of  $J$  to  $\varphi_{J,0}^x$ , we had to draw on an approximate analytical calculation which may be another source for the small differences between the results obtained from the two models. However, in practice the chosen parameters can only be adjusted to limited precision/accuracy on the machine such that slightly different problems from the intended ones are being solved [18]. Interestingly, the coupler element, which can be viewed as part of the environment and might be the source of additional noise, does not cause significant deviations in the results compared to the results of the two-level description. This is definitely different from the errors caused by the resonators in the considered gate-based model in Ref. [2].

### C. Comparison to D-Wave 2000Q data

Because we find good agreement between the system described by the Hamiltonian Eq. (11) and the 2-level system, we compare the success probability for both these systems with the percentage of successful runs on the D-Wave 2000Q quantum annealer. In Appendix A (see Table III), we present the data obtained by 10 repetitions of annealing simultaneously, 992 copies of the two-qubit problems distributed over the D-Wave 2000Q chip, for an annealing time  $t_a = 20 \mu\text{s}$ . We find that although the annealing time on the D-Wave is much larger than for our simulations ( $20 \mu\text{s}$  instead of  $5 \text{ns}$ ), a large fraction of the D-Wave data seems to agree (approximately) with the

TABLE II. Percentage for finding the ground state (GS) on D-Wave's DW\_2000Q\_2 chip for three different problem instances and four different annealing times. The minimal and final gap (in GHz) are denoted by  $\Delta E$  and  $\Delta_p$ , respectively.

Case	$J$	$h_1$	$h_2$	$\Delta E$	$\Delta_p$	GS probability in %			
						$1 \mu\text{s}$	$20 \mu\text{s}$	$100 \mu\text{s}$	$1 \text{ms}$
(a)	0.1	0.3	-0.3	5.481	14.07	92.5	96.2	97.6	98.5
(b)	-1	0	0.05	1.206	3.519	63.0	65.6	67.1	69.7
(c)	-1	0.96	0.94	0.627	1.407	51.4	52.9	53.6	55.6

corresponding ground-state probabilities obtained from the simulation of the SQUID model Eq. (11) and its two-level approximation. This agreement is probably accidental. The annealing time of  $5 \text{ns}$  was chosen to keep the real time to solve the TDSE of the SQUID model within acceptable limits as well as having some variation in the ground-state probability at the end of the annealing process without having to use too small values for, or differences between, the parameters  $J$  and  $h_i$ . In spite of the large difference in annealing times, the good agreement suggests that in the D-Wave device there are physical processes at work that affect the annealing, processes which are not incorporated in the SQUID model Eq. (11) or the corresponding two-level approximation Eq. (27).

Concrete evidence for the relevance of such processes is shown in Table II, where we present D-Wave data for three different cases whose energy spectra are shown in Figs. 9(a)-(c). Because the spectra of these cases differ significantly, we assume that they are a representative subset of the cases studied previously. Data characterizing the problem instances such as the minimal energy gap  $\Delta E$  and the problem gap  $\Delta_p$  of the final Hamiltonian are listed in Table II as well as the frequency of runs finding the ground states ( $|\uparrow\downarrow\rangle$ ,  $|\downarrow\uparrow\rangle$ , and  $|\uparrow\uparrow\rangle$  for the three cases, respectively) on the D-Wave machine for four different annealing times. The results reported in Table II were obtained by putting 992 copies of the 2-spin problems on the Chimera-graph and performing 1000 annealing runs.

Table II shows some additional interesting facts. First, recall that for the shortest annealing time considered, i.e.,  $1 \mu\text{s}$ , simulation of the quantum annealing process in the 2-level description yields the ground state with probability one for the three listed cases. Clearly, as Table II shows, this is not the case for the D-Wave data, not even if we increase the annealing time to  $1 \text{ms}$ , as is most evident for case (c). We emphasize that these differences in the observed frequencies for finding the ground state are not due to poor statistics nor can they be attributed to the differences in the minimal gaps  $\Delta E$ . Correlating these observations with the energy level spectra shown in Fig. 9 suggests that the observed reduction of the frequency for finding the ground state may be related to the distribution of energy levels for  $s \rightarrow 1$ . But the mechanism that causes the observed reduction of frequencies when going from case (a) to (c) cannot be found within

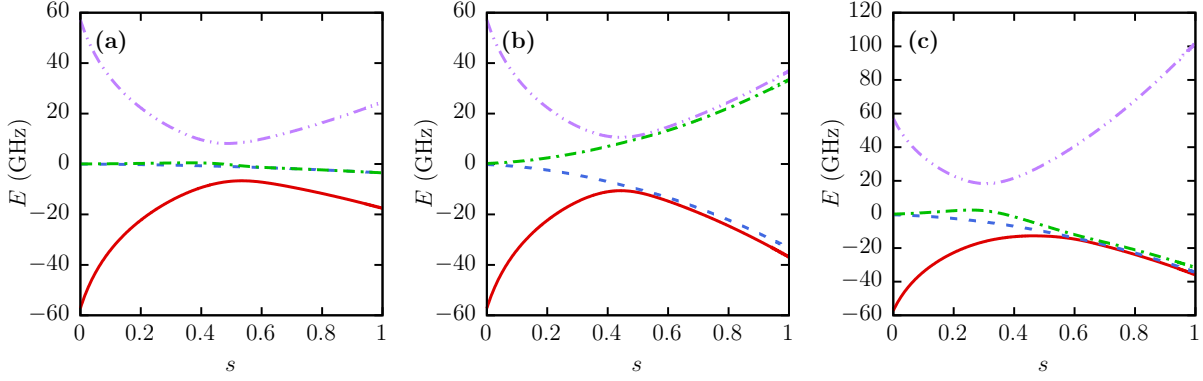


FIG. 9. (color online) Energy spectra during the annealing process for the three cases listed in Table II. (a) The case with parameters  $J = 0.1$ ,  $h_1 = 0.3$  and  $h_2 = -0.3$ ; (b) with parameters  $J = -1$ ,  $h_1 = 0$  and  $h_2 = 0.05$ ; (c) with parameters  $J = -1$ ,  $h_1 = 0.96$  and  $h_2 = 0.94$ .

the description of the quantum dynamics of the two-qubit system. Explaining these experimental observations requires considering additional physical processes.

The first process that comes to mind is the interaction of the qubits with their environment at non-zero temperature. In the next section, we address this issue by solving the TDSE of the two-spin model Eq. (27) coupled to a spin bath, complementing previous work that investigated the effects of finite temperature on quantum annealing [23–29].

## VII. SYSTEM COUPLED TO A BATH

The annealing process of the isolated two-qubit system may be understood in terms of the adiabatic theorem. However, in the real world, the two qubits are in contact with an environment at finite temperature. In this section, we scrutinize the extent to which the coupling to a heat bath, i.e., the presence of thermal fluctuations, affects the annealing process. This, we hope, may shed light on the annealing behavior observed on the D-Wave machine in the cases studied.

We do not assume the heat bath to be Markovian but instead we solve the TDSE of the whole system comprising the two-qubit system and the bath. In order to be able to perform such simulations, it is necessary to keep these models simple. Therefore, it would be remarkable to find good quantitative agreement between the results of the simulations and those obtained with the D-Wave machine. Thus, the goal here is limited to find out if such models can reproduce, qualitatively, the trends observed in the D-Wave data.

We model the heat bath as a collection of spin-1/2 objects which might represent e.g. defects in the material. We assume that this heat bath is at thermal equilibrium, with a temperature given by the operating temperature of the D-Wave machine. We denote the inverse of this operating temperature by  $\beta^* = 0.588$  ns (in units of  $\hbar = k_B = 1$ ), corresponding to a temperature of  $T = 13$  mK.

The Hamiltonian of the system (S) + bath (B) reads

$$\mathcal{H}(t) = H_S(s = t/t_a) + H_B + \lambda H_{SB}, \quad (36)$$

where  $\lambda$  controls the overall strength of the system-bath (SB) interaction. The time evolution during the quantum annealing process of the closed quantum system defined by Hamiltonian Eq. (36) is obtained by solving the TDSE given in Eq. (28) with the initial state

$$|\Psi(t=0)\rangle = |++\rangle \otimes |\Phi(\beta)\rangle. \quad (37)$$

The method to prepare the thermal state  $|\Phi(\beta)\rangle$  and other technical details are discussed in Appendix B.

The system Hamiltonian is given by

$$H_S = A(s)(-\sigma_1^x - \sigma_2^x) + B(s)(-J\sigma_1^z\sigma_2^z - h_1^z\sigma_1^z - h_2^z\sigma_2^z), \quad (38)$$

and changes with time as a function of the annealing variable  $s = t/t_a$ . We consider two extreme cases for  $H_B$  and  $H_{SB}$ .

### A. Model I

In the first case, the bath is modeled as a ring of spins represented by the Pauli matrices  $\boldsymbol{\mu}_n = (\mu_n^x, \mu_n^y, \mu_n^z)$ , described by the Hamiltonian

$$H_B = -K \sum_{n=1}^{N_B} (r_n^x \mu_n^x \mu_{n+1}^x + r_n^y \mu_n^y \mu_{n+1}^y + r_n^z \mu_n^z \mu_{n+1}^z). \quad (39)$$

Here and in the following  $N_B$  denotes the number of bath spins. The couplings  $r_n^x$ ,  $r_n^y$ , and  $r_n^z$  are taken to be uniform random numbers in the range  $[-1, +1]$  and  $K$  determines the spectral range of  $H_B$ . For random couplings it is unlikely that the model Eq. (39) is integrable (in the Bethe-Ansatz sense) or has any other special features such as conserved magnetization etc. The bath Hamiltonian Eq. (39) with random couplings has the property

that the distribution of nearest-neighbor energy levels is Wigner-Dyson-like [30, 31]. Extensive simulation work on spin-baths with very different degrees of connectivity [32] suggests that as long as there is randomness in the system-bath coupling and randomness in the intra-bath coupling, the simple model Eq. (39) may be considered as a generic spin bath [30, 31]. The Hamiltonian describing the interaction of the two-spin system with the bath is taken to be

$$H_{\text{SB}} = -r_{n,1}^x \mu_n^x \sigma_1^x - r_{n,1}^y \mu_n^y \sigma_1^y - r_{n,1}^z \mu_n^z \sigma_1^z \\ - r_{m,2}^x \mu_m^x \sigma_2^x - r_{m,2}^y \mu_m^y \sigma_2^y - r_{m,2}^z \mu_m^z \sigma_2^z, \quad (40)$$

where  $n$  and  $m$  are chosen randomly from the set  $\{1, \dots, N_B\}$  such that  $n \neq m$ . The  $r_{n,1}^\alpha$  and  $r_{m,2}^\alpha$  are real-valued random numbers in the range  $[-1, +1]$ .

### B. Model II

In this case, the bath is modeled as a collection of non-interacting two-level systems given by the Hamiltonian

$$H_B = -\Omega \sum_{n=1}^{N_B} r_n^x \mu_n^x + r_n^y \mu_n^y + r_n^z \mu_n^z, \quad (41)$$

where the parameter  $\Omega$  together with the random numbers  $r_n^x, r_n^y, r_n^z \in [-1, 1]$ , determine the level splitting of each spin. The interaction between the qubits and the bath spins is chosen such that each qubit interacts with a different half of the spin bath. This type of interaction is modeled by the Hamiltonian

$$H_{\text{SB}} = \sum_{\alpha=x,y,z} \left[ \sigma_1^\alpha \sum_{n=1}^{N_B/2} r_{n,1}^\alpha \mu_n^\alpha + \sigma_2^\alpha \sum_{n=N_B/2+1}^{N_B} r_{n,2}^\alpha \mu_n^\alpha \right]. \quad (42)$$

### C. Parameters

Obviously, to compare the simulation results with D-Wave results it is necessary to solve the TDSE for the same time interval as used on the D-Wave machine. In practice, this requirement puts a severe constraint on the size of the problems for which one can solve the TDSE within a reasonable amount of real time. Simulating the annealing process over  $1 \mu\text{s}$  (the shortest annealing time possible on the D-Wave machine) for a system comprising  $N_B = 16$  on a BullSequana X1000 supercomputer (JUWELS [33]) takes about 4 hours using 40 compute cores. Performing a simulation for  $N_B = 28$  bath spins takes about one week (400000 time steps of  $0.0025 \text{ ns}$  using 5120 compute cores). Earlier work which studied the TDSE dynamics of two spins coupled to a spin bath [31] shows that the results for  $N_B = 16$  and  $N_B = 28$  primarily differ in the statistical fluctuations on the data (see also Appendix B). Therefore, we have chosen to perform

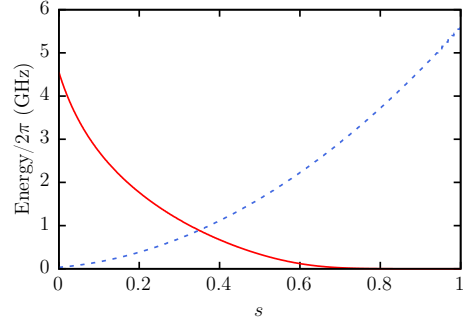


FIG. 10. (color online) Annealing schedule of the DW\_2000Q\_2 chip which was used for the simulation with the heat bath. Solid line (red) corresponds to  $A(s)$  and dashed (blue) line corresponds to  $B(s)$ .

most simulations with  $N_B = 16$ , repeating runs with different random numbers to collect statistics, and use a few runs with  $N_B = 28$  as an additional check on the data.

We use the annealing schedule of the DW\_2000Q\_2 chip (see Fig. 10) which is the machine that we used for our experiments.

In the case of model I, the initial state of the bath is prepared by projection with the operator  $\exp(-\beta H_B) = \exp(-\beta K(H_B/K))$ , as explained in Appendix B. From Eqs. (B2) and (B3), it is clear that spin baths with the same  $\beta K$  (and the same  $r$ 's, see Eq. (39)) will have the same thermal equilibrium properties. Therefore, we may use  $K$  as an adjustable parameter to “calibrate” the temperature of the spin bath with respect to the operating temperature of the D-Wave machine on which we performed our experiments. For instance, for a fixed choice of the  $r$ 's, spin baths with  $(\beta = 0.2 \text{ ns}, K = 5 \text{ GHz})$  and  $(\beta = 0.6 \text{ ns}, K = 5/3 \text{ GHz})$  have the same thermal properties. On the other hand,  $K$  sets the time scale of the spin-bath dynamics. Simulations with  $K$  in the range  $[1 \text{ GHz}, 5 \text{ GHz}]$  (data not shown) reveal that the primary quantity of interest, the ground-state probability of the two-qubit system at  $s = 1$ , does not change significantly with  $K$  (in the mentioned range, and for the same value of  $\lambda$ ). This leaves only the system-bath interaction  $\lambda$  as a parameter to fit the simulation data to the D-Wave data.

In the case of model II,  $\Omega$  plays the role of  $K$  in model I, i.e.,  $\beta\Omega$  determines the thermal equilibrium properties of the bath. Note that for modest values of  $N_B$ , model II is too simple to act as a genuine heat bath, but as a model for a few defects interacting with the SQUIDS, it can be a realistic choice [34–36]. Therefore, in this case, we set  $\beta \approx \beta^*$  and use  $\Omega$  and  $\lambda$  as fitting parameters.

### D. Comparison to D-Wave 2000Q data

Figures 11(a)-(c) depict the results of the simulation with the heat bath (bullets) averaged over ten different random initializations of the heat bath with  $N_B = 16$ . Results for  $N_B = 28$  (asterisks) show that for each

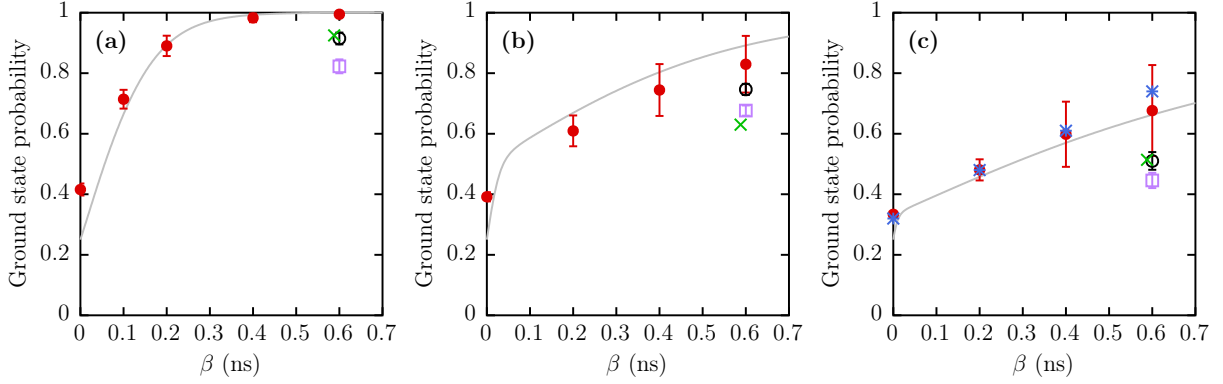


FIG. 11. (color online) Ground-state probability for three different problem instances (a)  $J = 0.1$ ,  $h_1 = 0.3$  and  $h_2 = -0.3$ , (b)  $J = -1$ ,  $h_1 = 0$  and  $h_2 = 0.05$ , (c)  $J = -1$ ,  $h_1 = 0.96$  and  $h_2 = 0.94$  as a function of the inverse temperature  $\beta$  with annealing time  $t_a = 1\mu\text{s}$ . Data points are averages over 10 simulation runs with different initializations of the heat bath described by model I with parameters  $K = 5\text{ GHz}$ ,  $\lambda = 0.8\text{ GHz}$  and  $N_B = 16$  (red bullets), by model II for  $\Omega = 0.125\text{ GHz}$  and  $\lambda = 1\text{ GHz}$  (black circle) and  $\lambda = 1.5\text{ GHz}$  (purple square). Error bars indicate the standard deviation. Results for  $N_B = 28$  (blue asterisks) are for the same parameters as the red bullets but for a single sample. The solid line (gray) shows the ground-state probability in thermal equilibrium as a function of the inverse temperature  $\beta$ . The cross represents the D-Wave result with annealing time  $t_a = 1\mu\text{s}$ , see Table II.

value of  $\beta$ , the averages of 10 samples of  $N_B = 16$  data are in good agreement with the data obtained from one  $N_B = 28$  sample. The solid line indicates the ground-state probability  $p_0$  of the isolated 2-level systems in thermal equilibrium for  $H_S$  at  $s = 1$ , i.e.,  $p_0 = \exp(-\beta E_0)/Z$  where  $E_0$  is the ground-state energy and  $Z = \text{Tr}(\exp(-\beta H_S))$  is the partition function. Qualitatively, the simulation data obtained using model I (bullets) nicely match the equilibrium line. The deviations from the equilibrium line may be due to the freeze-out where thermal transitions stop [29] and/or too short annealing times and/or the “magnetic Foehn” effect [37]. However, the simulation data do not match the data generated on the D-Wave machine (crosses). Assuming that the 2-level system on the D-Wave machine is in thermal equilibrium, we would infer from Figs. 11(a) to (c) that  $\beta \approx 0.2\text{ ns}$ , which is about a factor of three smaller than the inverse operational temperature of about  $\beta^* = 0.588\text{ ns}$ .

For model II, we have searched the parameter space  $1/8\text{ GHz} \leq \Omega \leq 2\text{ GHz}$ ,  $1/2\text{ GHz} \leq \lambda \leq 2\text{ GHz}$  for sets of  $(\Omega, \lambda)$  which would fit the D-Wave results best. These data are shown in Figs. 11(a)-(c) as open circles ( $\Omega = 0.125\text{ GHz}$ ,  $\lambda = 1\text{ GHz}$ ) and open squares ( $\Omega = 0.125\text{ GHz}$ ,  $\lambda = 1.5\text{ GHz}$ ). For cases (a) and (c) (see Table II), the former fit remarkably well to the D-Wave data. However, we have not found a set  $(\Omega, \lambda)$  which fits all D-Wave data very well.

## VIII. SUMMARY

We simulated the full system of three SQUIDs resembling two qubits and one tunable coupler element as used in the quantum annealer built by D-Wave Systems Inc.

and found that the higher energy levels as well as the presence of the coupler element have observable effects on the annealing process which, however, do not have a strong influence on the final success probability compared to the ideal 2-level system. In contrast to the investigation of the influence of the higher levels and resonators present in current systems for gate-based quantum computing [2], we found that, apart from a few exceptions, the effects are small for the examined cases of quantum annealing.

Furthermore, we investigated in detail the derivation of the 2-level representation to obtain expressions for  $\varphi_i^x$  and  $J$  that led to satisfying results (see Figs. 5 - 8). The simulation results are in good agreement with effects encountered in this derivation such as the change in the annealing scheme depending on the choice of  $\varphi_{j,0}^x$  which is also supported by findings in experiments [11].

Simulation data for the SQUID model Eq. (11) and the corresponding two-level approximation Eq. (27) for an annealing time  $t_a = 5\text{ ns}$  show remarkably good agreement with the D-Wave data obtained with an annealing time  $t_a = 20\mu\text{s}$ , also in those cases for which the probability for finding the ground state is substantially less than one. Although this agreement might be accidental, it suggests that the dynamics of the D-Wave quantum annealer is more complicated than what can be described by a closed-system model of the SQUIDs including higher levels.

Therefore, as a first step, we have studied quantum annealing in the presence of a heat bath. We solve the TDSE of the two-qubit system (Eq. (27)) + spin bath (Eq. (39)) for three cases with qualitatively different energy spectra of the two-qubit system, see Fig. 9. Comparing D-Wave and simulation results for an annealing time of  $1\mu\text{s}$ , we found that the simulation data for the

ground-state probabilities of the two-spin systems quite nicely agree with the corresponding thermal equilibrium values but also that these probabilities are significantly larger than those obtained with the D-Wave annealer. We have not found a common set of parameters ( $\beta, K, \lambda$ ) of the two-qubit - spin bath model that reproduces the D-Wave results for the three different cases considered.

Modeling the environment as a collection of non-interacting two-level defects, see Eq. (41), was found to yield a much more appropriate description of the D-Wave data. Although we could readily find values of the bath parameters  $\Omega$  and  $\lambda$  for which the solution of the TDSE yields results that are in excellent agreement with D-Wave data for two of the three different cases considered, we could not find a similar level of agreement with this data for all three cases if we impose the elementary requirement that the bath parameters  $\Omega$  and  $\lambda$  do not depend on the  $J$ 's and  $h$ 's that define the problem Hamiltonian.

Unlike in the case of a time-independent problem, the exchange of energy between the two qubits in the time-dependent (annealing) field and the spin bath seems to be an intricate process which, according to our simulation data, depends on the model parameters in a complicated manner. We leave a detailed study of this challenging problem for future research.

## ACKNOWLEDGMENTS

We would like to thank Mauricio Reis of D-Wave Systems Inc. for providing us with technical information and Seiji Miyashita for helpful discussions.

Access and compute time on the D-Wave machine located at the headquarters of D-Wave Systems Inc. in Burnaby (Canada) were provided by D-Wave Systems Inc.

The authors gratefully acknowledge the Gauss Centre for Supercomputing e.V. (www.gauss-centre.eu) for funding this project by providing computing time on the GCS Supercomputer JUWELS at Jülich Supercomputing Centre (JSC).

D.W. is supported by the Initiative and Networking Fund of the Helmholtz Association through the Strategic Future Field of Research project "Scalable solid state quantum computing (ZT-0013)".

## Appendix A: Data

Table III contains a list with the parameters  $h_i$  and  $J$ , the minimal energy gap  $\Delta E$ , and the success probabilities for the problems used to generate Fig. 8.

TABLE III. Parameter values of the problems shown in Fig. 8. a) Success probability for the 2-level system ( $t_a = 5\text{ns}$ ) b) success probability for the full model ( $t_a = 5\text{ns}$ ) c) percentage of successful runs on D-Wave's DW\_2000Q\_2 and DW\_2000Q\_2.1 chips ( $t_a = 20\mu\text{s}$ ).

$h_1$	$h_2$	$J$	minimal gap $\Delta E$ in GHz	success probability in %		
				a)	b)	c)
0.2	0.2	0.2	7.958914	99.9	99.5	99.7
0.2	-0.2	0	6.524809	99.8	99.6	95.8
0.3	-0.3	0.1	6.509859	99.9	99.6	90.6
0.1	-0.1	-0.1	4.817172	96.5	96.3	94.0
0.9	0.7	-1	4.660374	96.3	96.2	93.9
0.99	-0.8	1	4.367788	95.8	95.2	94.1
0.1	0.1	0	3.750846	93.0	92.8	80.5
0.3	0.3	-0.2	3.740396	96.2	96.2	81.4
0.07	-0.07	0	2.786031	82.1	81.6	66.8
0.07	0.07	0	2.786031	82.1	82.1	66.9
0.9	-0.8	1	2.766581	83.8	83.9	80.0
0.02	0.08	0.05	2.542547	77.7	77.6	71.2
0.99	-1	0.94	2.134413	84.8	57.9	48.3
0.05	0.05	0	2.092326	69.3	69.4	56.8
0	-0.05	0.05	1.585987	60.3	60.3	55.6
0	0.05	1	1.433807	69.0	67.6	64.4
0	0.05	-1	1.433807	69.0	69.1	65.3
0.01	0.04	0.025	1.419405	55.6	55.7	50.4
0.99	-1	0.96	1.366784	74.7	42.3	38.1
0.99	1	-0.96	1.366784	74.7	74.4	46.9
0.02	-0.02	-0.02	1.305954	51.1	50.6	43.8
0.02	0.02	0.02	1.305954	51.1	51.2	43.9
0.95	-0.99	0.98	1.145772	47.5	63.4	55.7
0.95	0.99	-0.98	1.145772	47.5	47.3	52.3
0.99	0.96	-1	1.018001	48.4	48.0	54.8
0.02	-0.02	0	0.939407	42.7	42.2	36.2
0	0.03	1	0.917871	61.8	60.8	59.0
0.96	-0.94	1	0.742309	50.7	57.5	55.1
0.96	0.94	-1	0.742309	50.7	50.0	54.0
0.98	-0.96	1	0.740480	45.4	56.3	53.4
0.98	0.96	-1	0.740480	45.4	44.7	51.0
0.01	-0.01	-0.01	0.716800	37.8	37.3	33.2
0.01	0.01	0.01	0.716800	37.8	38.0	33.9
0	0.02	-1	0.640932	57.9	57.8	57.0
0.01	0.009	0.002	0.543047	33.9	34.2	31.4
0.99	-1	0.98	0.510495	61.1	27.0	27.5
0.01	0.01	0	0.505201	33.5	33.8	31.7
0.99	-0.98	1	0.406202	35.3	49.3	47.2
0.99	0.98	-1	0.406202	35.3	34.6	45.6
0	-0.01	0.01	0.392828	33.0	33.2	31.6
0.005	0.005	0.005	0.388173	31.2	31.5	29.8
0.005	-0.005	-0.005	0.388173	31.2	30.7	29.1
0	0.01	1	0.343987	54.0	53.4	52.7
0	0.01	-1	0.343987	54.0	53.8	53.1
0.007	0	-0.01	0.302380	31.8	31.3	30.4
0.007	0	0.01	0.302380	31.8	32.0	30.5
1	0	-0.005	0.269309	54.0	53.1	52.8
1	0	0.005	0.269309	54.0	54.6	52.8
0.005	0.001	0.01	0.268263	31.4	31.6	30.2
0.005	-0.001	-0.01	0.268263	31.4	30.9	30.0
0.005	0	0.01	0.228548	30.9	31.2	29.6
0	0.005	0.5	0.193353	52.0	51.8	51.3
0	0.005	-0.5	0.193353	52.0	51.9	52.3
0.005	-0.001	0.01	0.187420	30.5	30.7	29.3
0.005	0.001	-0.01	0.187420	30.5	30.0	28.4
0	0.005	1	0.183074	52.0	51.5	50.7
0.005	0	-1	0.183074	52.0	51.8	50.7
0.003	0	0.01	0.145233	30.1	30.3	29.2
0	0.003	-1	0.114519	51.2	51.0	51.0
0	0.003	1	0.114519	51.2	50.8	50.1

## Appendix B: Numerical Solution of the TDSE

The numerical solution of the TDSE for a pure state of  $N_B + 2$  spins requires computational resources (memory and CPU time) proportional to  $2^{N_B+2}$ . For a brute force calculation of thermal expectation values  $\text{Tr } e^{-\beta \mathcal{H}} \mathcal{A}(t) / \text{Tr } e^{-\beta \mathcal{H}}$  this number changes to  $2^{N_B+2} \times 2^{N_B+2}$ . Fortunately, this increase in cost can be avoided by making use of “random-state technology” reducing the cost to that of solving the TDSE for one pure state [38]. If  $|\Phi\rangle$  is a pure state, picked uniformly from the  $D = 2^{N_B+2}$ -dimensional unit hypersphere, one can show that for Hermitian matrices  $X$  [38]

$$\text{Tr } X \approx D \langle \Phi | X | \Phi \rangle, \quad (\text{B1})$$

and that the statistical errors resulting from approximating  $\text{Tr } X$  by  $D \langle \Phi | X | \Phi \rangle$  are small if  $D$  is large [38]. For large baths, this property of the random pure state renders the problem amenable to numerical simulation.

In the case at hand, we proceed as follows. First we generate a thermal random state of the bath system, meaning that we compute the pure state

$$|\Phi(\beta)\rangle = \frac{e^{-\beta H_B/2} |\Phi\rangle}{\langle \Phi | e^{-\beta H_B} | \Phi \rangle^{1/2}}, \quad (\text{B2})$$

where  $\beta$  denotes the inverse temperature. For any bath observable  $\mathcal{A}(t)$  we have [38]

$$\langle \mathcal{A}(t) \rangle = \frac{\text{Tr } e^{-\beta H_B} \mathcal{A}(t)}{\text{Tr } e^{-\beta H_B}} \approx \langle \Phi(\beta) | \mathcal{A}(t) | \Phi(\beta) \rangle. \quad (\text{B3})$$

The initial state of the whole system is then a product state of the ground state of the two spins at  $s = 0$  and the thermal pure state  $|\Phi(\beta)\rangle$ , i.e.,

$$|\Psi(t=0)\rangle = |++\rangle \otimes |\Phi(\beta)\rangle. \quad (\text{B4})$$

Since the Hamiltonian Eq. (36) depends explicitly on time, we can only solve Eq. (28) numerically by time stepping. For this purpose, we use a Suzuki-Trotter product-formula based algorithm [39]. This algorithm employs a decomposition in terms of unitary matrices and is unconditionally stable by construction. All our simulations for the two qubits coupled to a heat bath were carried out with the massively parallel quantum-spin dynamics simulator (in house software), which is based on the same computational kernel as the massively parallel quantum computer simulator [40].

- 
- [1] M. A. Nielsen and I. L. Chuang, *Quantum Computation and Quantum Information: 10th Anniversary Edition* (Cambridge University Press, 2010).
  - [2] D. Willsch, M. Nocon, F. Jin, H. De Raedt, and K. Michielsen, Phys. Rev. A **96**, 062302 (2017).
  - [3] IBM, “IBM Q Experience,” <https://www.research.ibm.com/ibm-q/> (2016).
  - [4] M. Born and V. Fock, Z. Phys. **51**, 165 (1928).
  - [5] T. Kadowaki and H. Nishimori, Phys. Rev. E **58**, 5355 (1998).
  - [6] L. Landau, Physikalische Zeitschrift der Sowjetunion **2**, 46 (1932).
  - [7] C. Zener, Proc. R. Soc. London, Ser A **137**, 696 (1932).
  - [8] R. Harris, F. Brito, A. J. Berkley, J. Johansson, M. W. Johnson, T. Lanting, P. Bunyk, E. Ladizinsky, B. Bumble, A. Fung, A. Kaul, A. Kleinsasser, and S. Han, New J. Phys. **11**, 123022 (2009).
  - [9] R. Harris, M. W. Johnson, T. Lanting, A. J. Berkley, J. Johansson, P. Bunyk, E. Tolkacheva, E. Ladizinsky, N. Ladizinsky, T. Oh, F. Cioata, I. Perminov, P. Spear, C. Enderud, C. Rich, S. Uchaikin, M. C. Thom, E. M. Chapple, J. Wang, B. Wilson, M. H. S. Amin, N. Dickson, K. Karimi, B. Macready, C. J. S. Truncik, and G. Rose, Phys. Rev. B **82**, 024511 (2010).
  - [10] R. Harris, J. Johansson, A. J. Berkley, M. W. Johnson, T. Lanting, S. Han, P. Bunyk, E. Ladizinsky, T. Oh, I. Perminov, E. Tolkacheva, S. Uchaikin, E. M. Chapple, C. Enderud, C. Rich, M. Thom, J. Wang, B. Wilson, and G. Rose, Phys. Rev. B **81**, 134510 (2010).
  - [11] R. Harris, T. Lanting, A. J. Berkley, J. Johansson, M. W. Johnson, P. Bunyk, E. Ladizinsky, N. Ladizinsky, T. Oh, and S. Han, Phys. Rev. B **80**, 052506 (2009).
  - [12] S. Han, J. Lapointe, and J. E. Lukens, Phys. Rev. Lett. **63**, 1712 (1989).
  - [13] S. Boixo, V. N. Smelyanskiy, A. Shabani, S. V. Isakov, M. Dykman, V. S. Denchev, M. H. Amin, A. Y. Smirnov, M. Mohseni, and H. Neven, Nat. Commun. **7**, 10327 (2016).
  - [14] T. Lanting, A. J. Przybysz, A. Y. Smirnov, F. M. Spedalieri, M. H. Amin, A. J. Berkley, R. Harris, F. Altomare, S. Boixo, P. Bunyk, N. Dickson, C. Enderud, J. P. Hilton, E. Hoskinson, M. W. Johnson, E. Ladizinsky, N. Ladizinsky, R. Neufeld, T. Oh, I. Perminov, C. Rich, M. C. Thom, E. Tolkacheva, S. Uchaikin, A. B. Wilson, and G. Rose, Phys. Rev. X **4**, 021041 (2014).
  - [15] R. Harris, A. J. Berkley, M. W. Johnson, P. Bunyk, S. Govorkov, M. C. Thom, S. Uchaikin, A. B. Wilson, J. Chung, E. Holtham, J. D. Biamonte, A. Y. Smirnov, M. H. S. Amin, and A. Maassen van den Brink, Phys. Rev. Lett. **98**, 177001 (2007).
  - [16] A. M. van den Brink, A. J. Berkley, and M. Yalowsky, New J. Phys. **7**, 230 (2005).
  - [17] T. Albash, W. Vinci, A. Mishra, P. A. Warburton, and D. A. Lidar, Phys. Rev. A **91**, 042314 (2015).
  - [18] D-Wave Systems Inc., *Technical Description of the D-Wave Quantum Processing Unit* (2016).
  - [19] M. Suzuki, J. Math. Phys. **26**, 601 (1985).
  - [20] H. De Raedt, Comp. Phys. Rep. **7**, 1 (1987).
  - [21] Jülich Supercomputing Centre, Journal of large-scale research facilities **2** (2016), 10.17815/jlsrf-2-121.
  - [22] D-Wave Systems Inc., *private communication*.
  - [23] M. H. S. Amin, P. J. Love, and C. J. S. Truncik, Phys. Rev. Lett. **100**, 060503 (2008).
  - [24] J. Johansson, M. H. S. Amin, A. J. Berkley, P. Bunyk,

- V. Choi, R. Harris, M. W. Johnson, T. M. Lanting, S. Lloyd, and G. Rose, Phys. Rev. B **80**, 012507 (2009).
- [25] M. H. S. Amin, D. V. Averin, and J. A. Nesteroff, Phys. Rev. A **79**, 022107 (2009).
- [26] M. H. S. Amin, C. J. S. Truncik, and D. V. Averin, Phys. Rev. A **80**, 022303 (2009).
- [27] M. H. S. Amin and F. Brito, Phys. Rev. B **80**, 214302 (2009).
- [28] N. G. Dickson, M. W. Johnson, M. H. Amin, R. Harris, F. Altomare, A. J. Berkley, P. Bunyk, J. Cai, E. M. Chapple, P. Chavez, F. Cioata, T. Cirip, P. deBuen, M. Drew-Brook, C. Enderud, S. Gildert, F. Hamze, J. P. Hilton, E. Hoskinson, K. Karimi, E. Ladizinsky, N. Ladizinsky, T. Lanting, T. Mahon, R. Neufeld, T. Oh, I. Perminov, C. Petroff, A. Przybysz, C. Rich, P. Spear, A. Tcaciuc, M. C. Thom, E. Tolkacheva, S. Uchaikin, J. Wang, A. B. Wilson, Z. Merali, and G. Rose, Nat. Commun. **4**, 1903 (2013).
- [29] M. H. Amin, Phys. Rev. A **92**, 052323 (2015).
- [30] P. Zhao, H. De Raedt, S. Miyashita, F. Jin, and K. Michielsen, Phys. Rev. E **94**, 022126 (2016).
- [31] H. De Raedt, F. Jin, M. Katsnelson, and K. Michielsen, Phys. Rev. E **96**, 053306 (2017).
- [32] F. Jin, K. Michielsen, M. A. Novotny, S. Miyashita, S. Yuan, and H. De Raedt, Phys. Rev. A **87**, 022117 (2013).
- [33] Jülich Supercomputing Centre, Journal of large-scale research facilities **5** (2019), 10.17815/jlsrf-5-171.
- [34] A. Shnirman, G. Schön, I. Martin, and Y. Makhlin, Phys. Rev. Lett. **94**, 127002 (2005).
- [35] C. Müller, A. Shnirman, and Y. Makhlin, Phys. Rev. B **80**, 134517 (2009).
- [36] J. H. Cole, C. Müller, P. Bushev, G. J. Grabovskij, J. Lisenfeld, A. Lukashenko, A. V. Ustinov, and A. Shnirman, Appl. Phys. Lett. **97**, 252501 (2010).
- [37] K. Saito and S. Miyashita, J. Phys. Soc. Jap. **70**, 3385 (2001).
- [38] A. Hams and H. De Raedt, Phys. Rev. E **62**, 4365 (2000).
- [39] H. De Raedt and K. Michielsen, in *Handbook of Theoretical and Computational Nanotechnology*, edited by M. Rieth and W. Schommers (American Scientific Publishers, Los Angeles, 2006) pp. 2 – 48.
- [40] H. De Raedt, F. Jin, D. Willsch, M. Willsch, N. Yoshioka, N. Ito, S. Yuan, and K. Michielsen, Comput. Phys. Commun. **237**, 47 (2019).